energies

MDPI

Article

Fault-Tolerant Operation of Bidirectional ZSI-Fed Induction Motor Drive for Vehicular Applications

Vivek Sharma [1], Md. Jahangir Hossain [2] and Subhas Mukhopadhyay [1,*]

[1] School of Engineering, Macquarie University, Sydney, NSW 2109, Australia
[2] School of Electrical and Data Engineering, University of Technology Sydney, Ultimo, NSW 2007, Australia
* Correspondence: subhas.mukhopadhyay@mq.edu.au

Abstract: This paper presents an efficient and fast fault-tolerant control scheme for a bidirectional Z-source inverter (BiZSI)-fed induction-motor drive system for vehicular applications. The proposed strategy aims for the fault detection, localization and diagnosis of the proposed system during switch failures in the inverter module. Generally, power–semiconductor switch failures in inverter modules occur due to open- and short-circuit faults. An efficient modulation scheme is proposed and design specifications are thoroughly derived to obtain high voltage gains across the BiZSI network. A suitably fast detection and diagnosis scheme to isolate the faulty leg and resume the normal operation is discussed in this paper. The control scheme is provided such that the faulty leg is isolated and the motor phase is fed from a redundant leg to resume the operation. A feasible localization algorithm based on experimentally derived values and switching vectors is implemented. In addition, a fast fault diagnosis method based on current estimation and motor speed variation is designed and implemented. Moreover, the most important advantages of the proposed strategy include lower hardware requirements and less harmonic distortion in the output currents. Finally, the simulation and experimental results are presented to validate the feasibility of the theoretical analysis. An extensive performance evaluation of the proposed system with fault ride-through capabilities is performed to prove its suitability for vehicular applications. To validate its merits, the proposed strategy is compared with similar fault-tolerant schemes currently used in the industry.

Keywords: switch-faults; fault-tolerant; vehicular system; Z-source inverter; induction motor; IGBT

Citation: Sharma, V.; Hossain, M.J.; Mukhopadhyay, S. Fault-Tolerant Operation of Bidirectional ZSI-Fed Induction Motor Drive for Vehicular Applications. *Energies* **2022**, *15*, 6976. https://doi.org/10.3390/en15196976

Academic Editor: Rui Xiong

Received: 5 August 2022
Accepted: 15 September 2022
Published: 23 September 2022

1. Introduction

Modern transportation is currently experiencing major changes due to the development of electrified transportation technologies such as electric vehicles [1]. The implementation of induction-motor drives in vehicular applications has been an important part of this development. Induction motor drives are widely used across current industries due to their ruggedness, higher reliability, low price and universal availability. Moreover, they are preferred by car manufacturers because they become naturally de-excited in case of inverter fault and can be implemented to improve the safety characteristics of vehicular applications [2,3]. The simplified control methods of induction motors provide high performance and a fast dynamic response [4]. With advantages such as variable speed control, and variable frequency control, these drives are still popular. They are driven by conventional modules of dc–ac power conversion, namely a voltage-source inverter (VSI) and a current-source inverter (CSI) [5,6]. The implementation of these modules with induction-motor drives is presented in [7–11]. Due to the disadvantages of two-stage power conversion, limited ac output, and susceptibility to electromagnetic interference (EMI) noise, these conventional inverter modules are losing their popularity, especially in fault-tolerant control applications. A popular converter–inverter topology called an impedance-source inverter (ZSI) is in high demand due to its single-stage power conversion capability, and, thus, its high-efficiency [12–15]. It is a two-port network that has inductors and capacitors connected in an X-shape to couple the dc source to the inverter.

1.1. Motivation

The Z-source converter overcomes the conceptual and theoretical barriers and limitations of the traditional voltage-source converter and current-source converter. This network can be used for all dc-to-ac, ac-to-dc, ac-to-ac, and dc-to-dc power conversion. A comparative study of the VSI-, CSI-, and ZSI-fed induction-motor drive systems was performed in [16]. These studies validate the advantages of the ZSI over traditional inverter modules. However, with rising concerns over the safety of applications, the question of reliability has received increased attention. This research is of great interest to the automotive industry, as they follow a strict protocol of ensuring safety procedures during the operation of motor drives. Hence, the need for an efficient fault-tolerant scheme to cater to the needs of industries is a demanding challenge . However, the occurrence of faults, due to factors such as aging, the thermal rise of the windings of motors, and switch failures; is inevitable in practice. As per the available literature, switch failures contribute to the majority of fault instances in the drive system. Hence, this study aims to analyse and provide solutions for switch failures.

1.2. Literature Review

Various solutions based on several domains of control were suggested for fault-tolerant schemes in the literature. The basic idea of implementing this control involves monitoring changes in the electrical parameters of the system. Nevertheless, many fault-tolerant strategies for AC motor drives were suggested in [17–24]. In [17], the authors suggested isolation and reconfiguration of the faulted system based on a knowledge-base block Fault Identification System (FIS). The current sensor fault diagnosis based on independent observers is discussed in [18,25]. Studies [19,20] discussed the fault-tolerant operation and performance characteristics for six-phase and three-phase drive systems. The control schemes to compensate for DC link capacitor failure is explored in [24]. Furthermore, the performance of conventional voltage source inverters is studied for permanent magnet drives in [21]. With the goal of understanding current trends of fault-tolerant systems for vehicular applications, studies in [22,23] suggested the use of reliability analysis and fault-tolerant control strategies for electric vehicles. Additionally, surveys based on the effectiveness of various fault-tolerant schemes for motor drives were presented in [26–30]. These surveys listed a comparative analysis of the currently practiced fault-tolerant configurations, which include low-gain modulation schemes.

1.3. Research Gap and Contribution

The above literature highlighted that the conventional converter topologies do not suffice for the high voltage magnitude required for the motor drives. They also lack the integration of fast and effective methods for the identification, isolation, and reconfiguration of faults for vehicular applications. However, due to the ease of implementation, the majority of the literature suggested or achieved a fault-tolerant topology by implementing a redundant leg configuration. Additionally, during fault-tolerant control, the speed response of the motor drive did not receive much attention as a prime aspect. To address the above-mentioned issues, in this paper, a fault-tolerant BiZSI-fed induction-motor drive is proposed for switch failures. It is known that in case of motor drive applications, the torque-speed characteristics are essential. Hence, this study provides a more thorough analysis of the post-fault capability of the proposed induction motor drive with the mentioned characteristics. The major contributions of this experimental study are summarized as follows:

1. Design and implement a high-gain improved modulation strategy with economical network parameters to be fed to a Bidirectional Z-source network without the use of transformers.
2. Develop an efficient fault-tolerant strategy with suitable control measures to identify and locate the fault in the corresponding switch, which facilities fast detection, with a diagnosis time of less than one switching cycle, and validate the suitability of the achieved results for vehicular applications.

3. Evaluate and compare the performance of the proposed system under different operating conditions.

The proposed system provides excellent speed-torque performance; and with high power quality output, and it is highly efficient in post-fault operation (explained in Section 6). The proposed diagnosis strategy is characterized by an improved performance and quickness in action compared to currently practiced strategies (explained in Section 7). The authors would like to highlight that this research is unique in the following aspects:

- Design and implementation of a new modulations scheme which outperforms the previous methods in terms of high output voltage gain and lower complexity in control scheme that provides excellent speed-torque performance, and with high power quality output.
- Incorporation of a new fault localization algorithm based on switch vector with a suitable fault tolerant scheme.
- Inclusion of an improved speed controller with the proposed fault-tolerant strategy that facilitates a shorter diagnosis and recovery time in comparison with conventional fault-tolerant strategies implemented in the industries.

The rest of the paper is organized as follows. Section 2 presents the detailed modeling of the proposed system. It consists of a Bi-directional Z-source inverter and an induction motor. The proposed fault-tolerant strategy is discussed in Section 3. Subsequently, simulation results based on the proposed fault-tolerant strategy are presented in Section 4. The validation of the theoretical discussions is achieved by experimental tests described in Section 5. The suitability of the achieved results for vehicular applications is discussed in Section 6. Section 7 presents a comparison of the proposed fault-tolerant strategy with similar strategies utilized in the current industry to prove the effectiveness of the proposed strategy. Finally, the conclusion is presented in Section 8.

2. Modeling of the Proposed System

This section aims to discuss the modeling of the overall system comprising of design specifications suitable for the proposed high-gain modulation scheme of the BiZSI, and modeling of the induction motor to facilitate fault-tolerant operation. It consists of mathematical analysis of the current estimation parameters and design of the speed control loop to maintain the speed-characteristics of the motor during post-fault operation. The basic circuit diagram of the proposed system is shown in Figure 1.

The general system consists of a battery source with a bidirectional switch (IGBT) and an LC impedance network in an X-shape connected to an inverter module. The whole arrangement is fed to the three-phase induction motor. Based on the industrial application of the proposed system, the bidirectional switch is added to facilitate the discontinuous mode of operation. The bidirectional switch works on command to allow power flow from source to load and load to source. The four-quadrant operation of the Z-source network allows bidirectional power flow between the input dc source and the inverter by keeping the polarity of the dc current on the inverter side while changing the polarity of the applied voltage. The phase angle ϕ between the output voltage and the source voltage will be used to control the direction of the power flow between the input and the load. During experimentation, the bidirectional flow is achieved by controlling the firing angle of the inverter corresponding to the rectification and inversion mode. If the firing angle $\alpha > 90^{\circ}$, the inverter works in the inversion mode, and vice-versa. The detailed modeling of the proposed system is explained below.

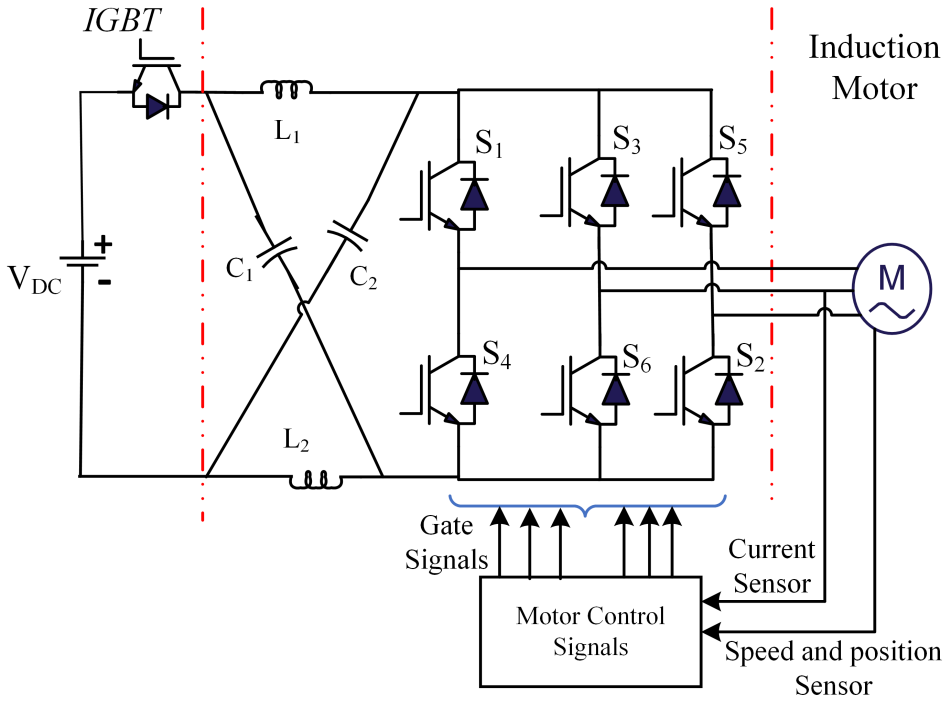

Figure 1. Generic schematic of a motor control scheme.

2.1. Bidirectional-Z-Source Network

The maximum output across the impedance network can be obtained by an efficient modulation scheme and selecting suitable design parameters.

2.1.1. Modulation Scheme

The traditional modulation schemes for impedance networks are explained in [31–35]. In order to obtain high gain, the modulation scheme should account for six active states and converting the zero states into shoot-through states. It facilitates the smooth transition between the shoot-through and non-shoot through states. The switching logic diagram of the proposed modulation scheme is shown in Figure 2. It is obtained by comparing a sinusoidal waveform with a triangular carrier.

These specified switching cycles are selected based on the state-space model of the impedance network [36]. The state model of the Bi-ZSI for the selection of the proposed modulation scheme during active and zero states is given as [37]:

$$\begin{aligned} L_1(\frac{di_{in}}{dt}) + M(\frac{di_2}{dt}) &= V_s - V_{c1}(1-u) + V_{c2}u \\ L_2(\frac{di_2}{dt}) + M(\frac{di_{in}}{dt}) &= V_{c2}(1-u) + V_{c1}u \\ C_1(\frac{dV_{c1}}{dt}) &= -i_2 u + i_{in}(1-u) - I_{L0}(t)(1-u) \\ C_2(\frac{dV_{c2}}{dt}) &= -i_{in} u + i_2(1-u) - I_{L0}(t)(1-u) \end{aligned} \quad (1)$$

where L_1, L_2, C_1, and C_2 are inductances and capacitances of the Z-source network; M is the mutual inductance; and u defines the command-signal variable.

The command-signal variable u is defined here to represent the state of the inverter, specifically, whether it is short circuited or not, i.e., $u = 1$, when the inverter is shortened.

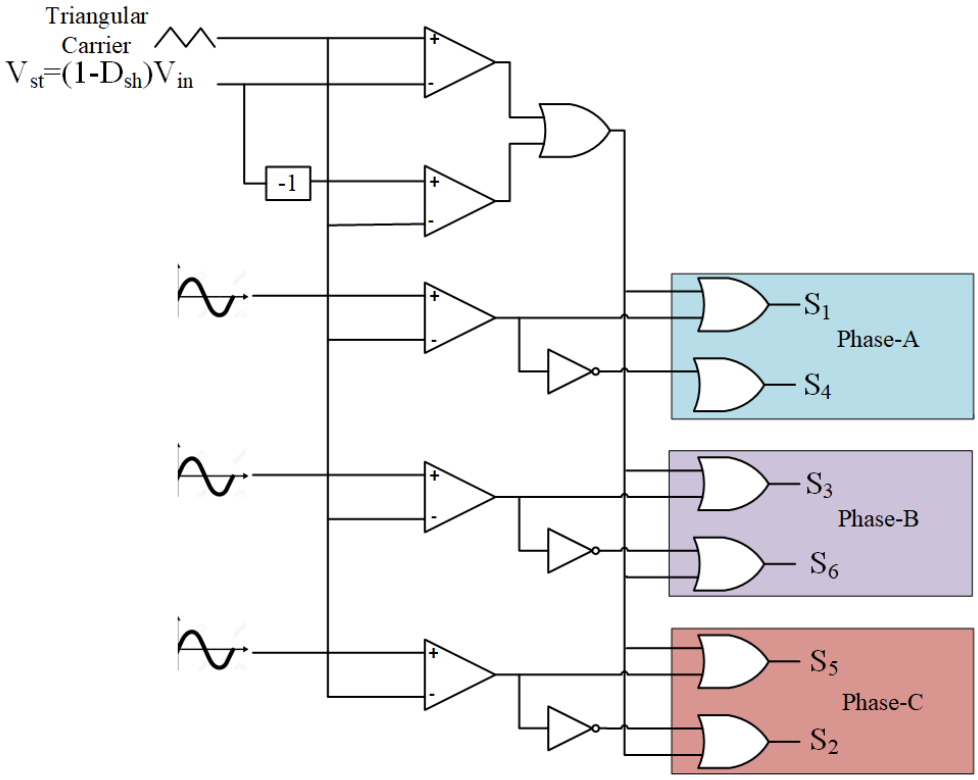

Figure 2. Proposed modulation scheme.

The selected modulation should account for safe shoot-through states across the Z-source network. These shoot-through states boost the dc link voltage within the specified switching cycle. With the requirement of a high voltage gain, the proposed modulation scheme is obtained with a boosting factor (B) calculated as [38,39]:

$$B = \frac{\pi}{3 - \pi(1 - K)} \tag{2}$$

The overall gain can be determined as [12,13,40]:

$$G = \frac{\pi/\sqrt{3}}{3 - \pi(1 - K)} \tag{3}$$

where K is the factor to control the shoot-through periods.

For the proposed modulation scheme, the gain G is controlled by varying duty cycle (D) and modulation index (M). The duty cycle of shoot-through mode is related to the modulation index as: $D \leq 1 - M$. The derived boost factor (B) in Equation (2) shows that the B can vary in $(1, \infty)$. In the case of a high value of D, the modulation index (M) should be a small value. However, operating at a lower modulation index can lead to high total harmonic distortion (THD) and low power quality. The boosting ratio is restricted in conventional ZSI. The proposed system uses over-modulation in order to facilitate high-output inverter gain because the amplitude of the modulating sinusoids is higher. This phenomenon is useful in reducing the Total Harmonic distortion of the output voltage which is studied in Section 6. However, by utilizing the proposed modulation scheme, a high gain is obtained by appropriately selecting the factor K in Equations (2) and (3). It is worth highlighting that due to the proposed modulation scheme, the achieved boost factor is 2.7.

The efficacy of the proposed modulation scheme is explored against currently utilised conventional modulation schemes. From Equations (2) and (3), it is found that the voltage

gain of the proposed Z-source network is dependent on the shoot-through duty cycles, which are obtained through the modulation scheme. Figure 3 shows a comparison of the performance of the proposed modulation scheme with that of traditional modulation schemes in terms of voltage gain.

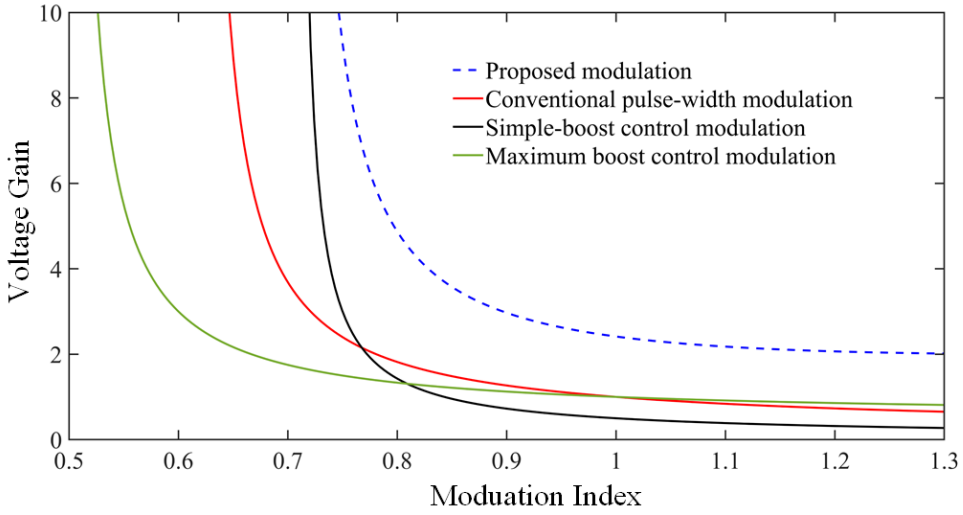

Figure 3. Voltage gain comparison.

These plots are obtained through a MATLAB/Simulink model of the proposed system. The results are verified through a comparative study with the published literature [37,41,42]. As mentioned earlier, it is a known fact that the power quality of the output gain is associated with the modulation index and a ripple-free output can be achieved with a higher modulation index. It can be seen from Figure 3 that the voltage gain of the proposed Bi-ZSI is higher than most of the compared topologies within a specified range of the modulation index. For a higher modulation range of 0.9–1.2, the proposed scheme shows a higher voltage gain of 2.5–3. Therefore, to achieve the same voltage gain, the proposed system can operate with higher modulation index which is not possible with the compared topologies. Furthermore, it is shown in Figure 3 that a linear high-voltage gain is obtained due to the proposed modulation scheme, which is essential for the high starting torque of the motor drive.

Furthermore, a comparative analysis of the proposed modulation scheme with the conventional modulation technique is listed in Table 1 to highlight the advantages and efficacy of the proposed scheme. Apart from the high boost ability, the proposed scheme facilitates lower voltage stresses on the capacitors C_1 and C_2 for the same voltage gain. This will result in high performance even with components having a small size and low power rating. Furthermore, the effect of peak value of transient overvoltage is taken into account. The voltage stress across the IGBTs is low due to the proposed modulations scheme, which results in reduced values of transients in the system. Additionally, the capacitor voltage ripples are assessed for the conventional and proposed modulation schemes. It is achieved by adding a step disturbance of ± 0.02 to the modulation index for a range of voltage gains (0, 10). It is observed that the capacitor voltage ripple is lower with the proposed modulation technique. The effect of peak transients during shoot-through cycle is negligible.

Table 1. Comparison parameters of Modulation Scheme.

	Proposed	[43]	[37]	[42]	[32]	[33]
Number of Reference Signals	3	5	3	4	3/4	3/4
Boost Factor	2.7	1.5	1.7	2.5	2	2.5
Voltage Gain	$\frac{M}{2M-1}$	$1-(\frac{3\sqrt{3}M}{2\pi})$	$\frac{1}{3\sqrt{3}-1}$	$\frac{4\pi M}{9\sqrt{3}M-2\pi}$	$\frac{M}{2\sqrt{3}M-2}$	$\frac{\pi}{3\sqrt{3}M-\pi}$
Maximum Voltage Stress	$\frac{2G-1}{\pi}$	$\frac{9\sqrt{3}G-4\pi}{2\pi}-1$	$\frac{2\pi}{3\sqrt{3}M}$	$\frac{2G-1}{G}\sqrt{\frac{G}{2G-1}}$	-	-
Peak transient Overvoltage on Upper IGBTs	1.1 pu	2.3 pu	2.4 pu	2 pu	1.0 pu	1.2 pu
Peak transient Overvoltage on Lower IGBTs	1.2 pu	2.3 pu	2.6 pu	<2 pu	-	-
Capacitor Voltage Ripple (CVR)	Low	High	High	Low	Low	Low
Switching Device Power (SDP)	Low	Low	High	Medium	Low	Low
Filter Requirement	Low	Bulky	Bulky	Low	Low	Low

The integration of a Bi-Z-source converter with the inverter is a vital part of the proposed system. The Switching Device Power (*SDP*) of a switching device is an important parameter for such configurations. SDP is expressed as the function of voltage and current stress across the switching devices. It is given as:

$$SDP = \sum_{i=1}^{N} V_i I_i \tag{4}$$

where V_i, I_i are the peak voltage and current across ith switching device, N is number of switching device.

The SDP of the proposed system is relatively low by utilizing the proposed modulations scheme. This is because the proposed modulation scheme ensures an excellent voltage transfer ratio with high power quality. With high power quality, the filter requirement is also low for the proposed system. This results in design advantages such as stability in output and easily available components in terms of rating. These advantages are of importance in vehicular systems, since they provide the added advantage of low weight and volume. This modulation scheme is implemented and tested on a single-phase drive in [40,44]. In this paper, the above-mentioned modulation scheme is utilized for a three-phase motor drive application.

2.1.2. Calculation of the Bi-ZSI Network Parameters

The design of inductors (L_1 and L_2) and capacitors (C_1 and C_2) is to be done in accordance with the current-handling capacity during the shoot-through states. The purpose of the inductors is to limit the current ripple, and capacitors are placed to absorb the current ripple. This is designed to obtain a high-quality fundamental component of the sinusoidal output waveform. The network inductance $L_1 = L_2 = L$ and capacitance $C_1 = C_2 = C$ are calculated as:

$$C = \frac{I_o T_s (2V_m - V_0)}{2K_1 V_o (4V_m - V_0)} \tag{5}$$

$$L = \frac{V_o T_s (2V_m - V_0)}{2K_2 I_o (4V_m - V_0)} \tag{6}$$

where V_m is the peak value of the line voltage, which is a multiple of the input voltage V_{in} given as:

$$V_m = \frac{MBV_{in}}{2} \tag{7}$$

where M is the modulation index.

According to Equations (2), (3), (5) and (6), the parameters of the Bi-ZSI are calculated and listed in Table 2.

Table 2. Design Parameters of the Bi-ZSI.

S. No.	Symbol	Device	Parameter Value
1	V_{in}	Source voltage	150 V
2	V_{out}	Output voltage	400 V
2	C_1, C_2	Capacitors of the Bi-Z-source	1000 µF
3	L_1, L_2	Inductors of the Bi-Z-source	3.3 mH
4	f	Line frequency	50 Hz
5	f_s	Switching frequency	5 kHz

2.2. Induction Motor

The design of fault-tolerant schemes for the complete system is based on rotor-current estimation and motor-speed estimation. The measurement of the parameters is performed as follows:

2.2.1. Current Estimation

A three-phase induction motor in the stationary $\alpha\beta$ reference frame is given by [45–47]

$$\frac{di_{s\alpha}}{dt} = -\frac{R_s L_r^2 + R_r L_m^2}{\sigma L_s L_r^2} i_{s\alpha} + \frac{L_m R_r}{\sigma L_s L_r^2} \psi_{r\alpha} + \frac{L_m \omega_r}{\sigma L_s L_r} \psi_{r\beta} + \frac{1}{\sigma L_s} u_{s\alpha} \tag{8}$$

$$\frac{di_{s\beta}}{dt} = -\frac{R_s L_r^2 + R_r L_m^2}{\sigma L_s L_r^2} i_{s\beta} + \frac{L_m R_r}{\sigma L_s L_r^2} \psi_{r\beta} - \frac{L_m \omega_r}{\sigma L_s L_r} \psi_{r\beta} + \frac{1}{\sigma L_s} u_{s\beta} \tag{9}$$

$$\frac{d\psi_{r\alpha}}{dt} = \frac{L_m R_r}{L_r} i_{s\alpha} - \frac{R_r}{l_r} \psi_{r\alpha} - \omega_r \psi_{r\beta} \tag{10}$$

$$\frac{d\psi_{r\beta}}{dt} = \frac{L_m R_r}{L_r} i_{s\beta} - \frac{R_r}{L_r} \psi_{r\beta} + \omega_r \psi_{r\alpha} \tag{11}$$

During the faulty operation, there is a high rise in the sinusoidal components in the $\alpha\beta$ reference frame. To facilitate the fault-tolerant control, the phase currents are measured. When phase-A current i_a is measured and found to be healthy, the observer shifts to other phases. The detection process goes on until a faulty leg is identified. If an error occurs in the measured value, the observer shifts the control to the fault-tolerant topology of the redundant leg. The observed error will be in terms of amplitude and rotation angle. The error in phase-A is linked to phase-B. The observer tries to converge the error values between the phases to bring the operation back to the normal value. The estimated states are given as:

$$\frac{di_{s\alpha}}{dt} = -\frac{R_s L_r^2 + R_r L_m^2}{\sigma L_s L_r^2} i_{s\alpha} + \frac{L_m R_r}{\sigma L_s L_r^2} \psi_{r\alpha} + \frac{L_m \omega_r}{\sigma L_s L_r} \psi_{r\beta} + \frac{1}{\sigma L_s} u_{s\alpha} + f(e_{is\alpha}) \tag{12}$$

$$\frac{di_{s\beta}}{dt} = -\frac{R_s L_r^2 + R_r L_m^2}{\sigma L_s L_r^2} i_{s\beta} + \frac{L_m R_r}{\sigma L_s L_r^2} \psi_{r\beta} - \frac{L_m \omega_r}{\sigma L_s L_r} \psi_{r\beta} + \frac{1}{\sigma L_s} u_{s\beta} + f(e_{is\beta}) \quad (13)$$

$$\frac{d\psi_{r\alpha}}{dt} = \frac{L_m R_r}{L_r} i_{s\alpha} - \frac{R_r}{l_r} \psi_{r\alpha} - \omega_r \psi_{r\beta} + g(e_{is\alpha}) \quad (14)$$

$$\frac{d\psi_{r\beta}}{dt} = \frac{L_m R_r}{L_r} i_{s\beta} - \frac{R_r}{L_r} \psi_{r\beta} + \omega_r \psi_{r\alpha} + g(e_{is\beta}) \quad (15)$$

where $e_{is\beta}$ and $e_{is\alpha}$ are current estimation errors, and f and g signify nonlinear functions of the $\alpha\beta$-axes.

2.2.2. Design of the Speed Control Loop

The proposed fault-diagnosis strategy is modeled in accordance to compensate for the speed drop during the event of faults. In this regard, a speed control lop is designed and fault is injected manually to identify whether the speed of the motor is brought back to rated value. The block diagram of the speed control loop is shown in Figure 4.

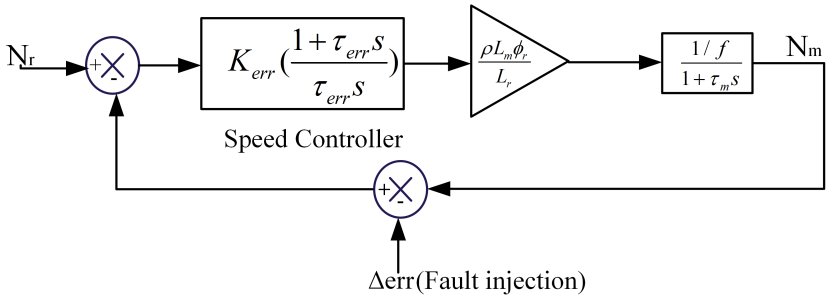

Figure 4. Speed control loop.

The electromagnetic torque developed in the motor is given as:

$$T_e = 1.5 p I_m \psi_s i_s \quad (16)$$

The dynamic model of the rotor depicting the change of mechanical speed is calculated as:

$$J\frac{d\omega_m}{dt} = T_e - T_l \quad (17)$$

During fault diagnosis, any variation in speed value is characterized by a finite difference between the rated speed and measured speed. This fault injection signal (Δ_{err}) is obtained by adding a constant positive value to the speed by the user. In this paper, a value of 10 rpm is added to the speed signal. This value is chosen by regular experimentation by adding positive values to the speed. The speed control loop shows a maximum deviation at 10 rpm for the proposed system and becomes unstable after this value. In the event of faults, the speed control block measures the error in the rated speed and identifies the dip in the value. Upon identification, the fault-tolerant strategy is implemented and the machine is brought back to the rated speed operation, which is shown in Section 6.

3. Fault-Tolerant Strategy

The fault-tolerant operation depends on the localization and diagnosis of the fault scenario. The circuit diagram for the proposed fault-tolerant topology is shown in Figure 5.

The proposed fault-tolerant strategy involves a four-output-pole inverter with the capability of isolating the faulty pole, while activating the fourth auxiliary pole (called the redundant leg) to resume the operation in the event of faults. In healthy condition, the redundant leg is non-operational. In case of faults, the redundant leg disconnects the faulty phase and restores the operation. This extra leg is connected to an isolation

circuit arrangement consisting of TRIACs, which isolate the faulty leg. This safety feature increases the reliability of the entire system. The inserting circuit, which consists of a TRIACs arrangement, is used to activate the redundant leg upon generation of a command signal due to a fault. The fault-tolerant approach is meant to maintain identical speed and torque characteristics for pre-fault and post-fault operation. Additionally, the accuracy and reliability of the fault-tolerant control should be efficient enough to have a speedy recovery, facilitating a smooth transition from faulty to normal operation. In this paper, the following permanent switch failures in the inverter module are considered:

(a) One switch open-circuited in one phase;
(b) Two switches open-circuited in one phase;
(c) One switch short-circuited in one phase;
(d) Two switches short-circuited in one phase.

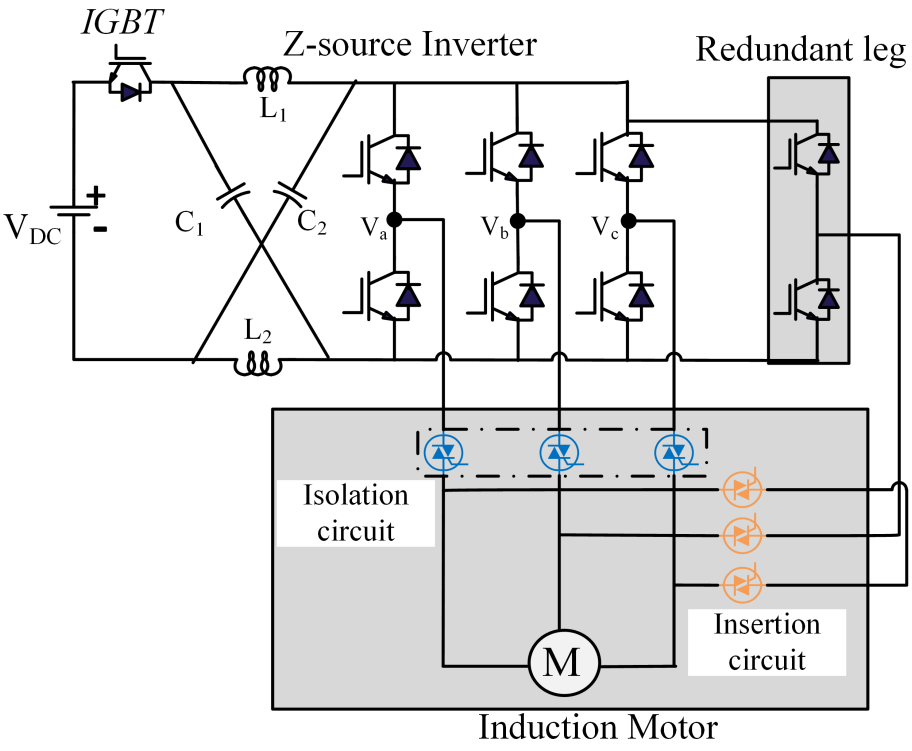

Figure 5. Circuit diagram of the Proposed system.

The above listed switch failures occur due to commonly occurring faults, i.e., open-and short-circuit faults. The proposed fault-tolerant operation consists of: (i) fault detection and localization, and (ii) fault-diagnosis for the post-fault operation which is explained in the subsequent subsections. Initially, the type of fault (open-circuit or short-circuit) is detected. Then, the faulty switch is identified and isolated to prevent the progression of the fault in the system. Finally, the fault diagnosis methodology enables the implementation of the redundant leg based on the proposed control scheme.

3.1. Fault Detection and Localization

The methods used to determine the nature and location of fault for the proposed system are detailed in this section. Correct and timely diagnosis can stop fault propagation over the entire system.

3.1.1. Open-Circuit Fault

The failure of the gate drive of an IGBT is often termed as open-circuit fault. It is caused by a driver fault or due to lifting of the connecting wires because of a thermal rise

in the device. It induces the dc component in the stator field and results in a pulsating torque. The overall torque available to the drive is reduced due to such a fault condition. Open-circuit faults can remain undetected in the system and degrade its power quality. Hence, it is necessary to have an efficient strategy to detect such faults quickly.

In this paper, open-circuit fault detection is performed by the normalized dc-current method, which is based on a diagnostic signature dependent on residuals. In this context, the residuals are the variables reflecting the deviation between the healthy and faulty condition. These variables are compared with appropriate thresholds, and the binary results of the comparisons form a diagnostic signature. The ultimate diagnostics rely on comparing the actual signatures with a set of reference signatures. Instead of using the fundamental components as the normalizing quantities, the average absolute values can be employed to determine the residuals value after comparisons. In healthy operation, the residuals are close to zero. With an open-circuit fault, the residuals are compared with a predefined threshold. The non-zero sample currents are considered to localize the fault. As the characteristics of this technique are independent of load, it is found to be the most efficient for variable speed drives. Upon the detection of faults, the faulty leg and switch need to be identified. To achieve this, a measurement of the normalized dc current is performed.

The fundamental components are obtained as [48]:

$$A_{abc1} = \frac{2\sum_{k=i-n+1}^{i} I_{abcav}(k\tau)cos(\frac{2\pi k}{n})}{n} \tag{18}$$

$$B_{abc1} = \frac{2\sum_{k=i-n+1}^{i} I_{abcav}(k\tau)sin(\frac{2\pi k}{n})}{n} \tag{19}$$

where i = 0, 1, 2, ∞, τ is the time constant, k is the number of states, n is the number of samples of currents, I_{abcav} is the average value of output current, and A_{abc1} and B_{abc1} are the fundamental components of the output currents.

The two components are essential to validate the low-order harmonic suppression by the proposed fault-tolerant technique. The normalized dc current is calculated as:

$$\gamma_{abc} = \frac{I_{abcav}}{\sqrt{{A_{abc1}}^2} + \sqrt{{B_{abc1}}^2}} \tag{20}$$

which is compared with a threshold value of 0.45 that is derived by a series of experimentation [49–52].

Under normal operation, the normalized value is equal to zero for a healthy inverter and close to ±1 in the case of a single fault on a leg. Hence, it is certain that the threshold value should be; 0 <threshold value< 1. The choice of threshold value is crucial to implement the diagnostic strategy as proposed in the paper. For instance, if the threshold is chosen to be 0.8, this method will be able to accommodate large asymmetries between the positive and negative half-cycles of the currents during transients. The distance of the threshold from unity, 0.45 (nearly half of unity) as considered, is a safety margin from the ±1 value of the faulty condition.

The sequence of fault detection is shown in Table 3, where γ_{anorm}, γ_{bnorm}, and γ_{cnorm} are the normalized values calculated from (20). The corresponding switch ($S_1 - S_6$) is located and considered as faulty, if the value specified in Table 3 is not satisfied.

Table 3. Open-circuit Fault Detection.

Switch	γ_a	γ_b	γ_c	γ_{anorm}	γ_{bnorm}	γ_{cnorm}
S_1	≤ 0			>0.45		
S_2		≤ 0			>0.45	
S_3			≤ 0			>0.45
S_4	>0			>0.45		
S_5		>0			>0.45	
S_6			>0			>0.45

3.1.2. Short-Circuit Fault

A high temperature overshoot, overvoltage, and high/wrong gate voltage are a few causes of short-circuit faults in the inverter module. A short-circuit fault may appear due to ionization and an uneven high-density current distribution. The high rise of the current during such faults damages the power semiconductor switches. Additionally, the IGBT gate-source capacitance will be affected by the short-circuit fault.

In this paper, the gate-voltage sensing method is used to detect and localize the short-circuit fault. The switch vector method proves to be an efficient strategy due to the presence of passive components in the proposed circuit. During a fault condition, the capacitance across the depletion region changes and affects the gate voltage. This lowers the gate current. Correspondingly, the gate voltage varies, and in turn, the fault can be detected. The changes in the gate voltage are noted and a fault diagnosis strategy is implemented in due time. To effectively locate the faulty switch, the switching-state estimation is proposed in case of a fault occurrence.

The ideal operation of the switches is considered in this operation. The states are defined for the upper- and lower-leg IGBTs. The switching states with the corresponding voltage vectors are shown in Table 4. The inverter can be modeled with phase voltage equations as:

$$v_{a0} = S_a V_d \tag{21}$$

$$v_{b0} = 2S_b V_d - V_d \tag{22}$$

$$v_{c0} = 2S_c V_d - V_d \tag{23}$$

where $S_{a,b,c}$ indicates switching states. The switching state is denoted as 1 if the upper switch conducts and 0 if the lower switch conducts.

The switching states listed in Table 4 aid in identifying the faulty switch/leg.

Table 4. Switching States and Voltage Vectors.

State	Switching State	Voltage Vector
1	$S_b = 0\ S_c = 0$	$v_0 = \frac{2V_d}{3}$
2	$S_b = 0\ S_c = 1$	$v_1 = \frac{V_d}{3} + j\frac{V_d}{\sqrt{3}}$
3	$S_b = 1\ S_c = 0$	$v_2 = \frac{-V_d}{3} + j\frac{-V_d}{\sqrt{3}}$
4	$S_b = 1\ S_c = 1$	$v_3 = -\frac{2V_d}{3}$

Upon locating the faulty switch/leg in the events of open-circuit or short-circuit faults, the gate signal of the corresponding switch/leg is blocked. The isolation and insertion circuit are activated to transfer the control to the redundant-leg devices. It should be noted that the changeover to the redundant leg does not change the topology of the system; hence, the modulation schemes and control algorithms remain unchanged. The basic flowchart of the fault-tolerant strategy is shown in Figure 6.

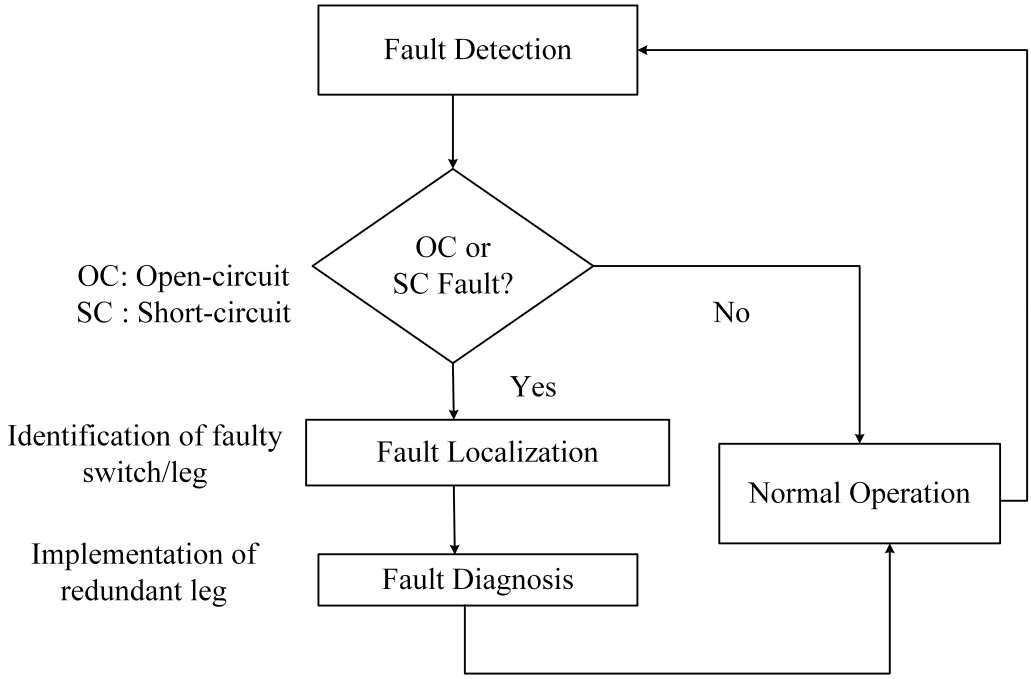

Figure 6. Flowchart of the Proposed fault-tolerant strategy.

3.2. Fault Diagnosis Methodology

To develop the fault diagnosis, adaptive observers are used to detect the fault occurrence. This is based on calculating the state estimation errors given by the observer. By comparing rotor reference frame Equations (8)–(11) with (12)–(15), the state estimation errors are obtained as:

$$\frac{de_{is\alpha}}{dt} = -\frac{R_s L_r^2 + R_r L_m^2}{\sigma L_s L_r^2} e_{is\alpha} + \frac{L_m R_r}{\sigma L_s L_r^2} e_{\psi r\alpha} + \frac{L_m \omega_r}{\sigma L_s L_r} e_{\psi r\beta} - f(e_{is\alpha}) \tag{24}$$

$$\frac{de_{is\beta}}{dt} = -\frac{R_s L_r^2 + R_r L_m^2}{\sigma L_s L_r^2} e_{is\beta} + \frac{L_m R_r}{\sigma L_s L_r^2} e_{\psi r\beta} - \frac{L_m \omega_r}{\sigma L_s L_r} e_{\psi r\alpha} - f(e_{is\beta}) \tag{25}$$

$$\frac{de_{\psi r\alpha}}{dt} = \frac{L_m R_r}{L_r} i_{s\alpha} - \frac{R_r}{l_r} e_{\psi r\alpha} - \omega_r e_{\psi r\beta} - g(e_{is\alpha}) \tag{26}$$

$$\frac{de_{\psi r\beta}}{dt} = \frac{L_m R_r}{L_r} i_{s\beta} - \frac{R_r}{L_r} e_{\psi r\beta} + \omega_r e_{\psi r\alpha} - g(e_{is\beta}) \tag{27}$$

The steady state time behaviours of the currents at the rated torque and speed are normal. In a three-phase induction motor, the stator flux vectors are meant to be a positive sequence. However, in case of a fault, the motor can continue running on the remaining two phases. The nature of the stator flux is affected and transformed into the negative-sequence component. This results in a pulsating torque. The above-modeled observer can estimate the stator current and rotor flux accurately. To track back to normal values of currents, the voltages at the redundant leg are compensated. The proposed control scheme to implement the fault-tolerant operation is shown in Figure 7.

The shoot-through compensation is provided by the feed-forward control facilitated by the proportional-integral (PI) controller. The gain function can be written as:

$$G(s) = \frac{(I_{load} R)(1 - 2D) + (I_{load} - I_{L1} - I_{L2})(L_s + R_s)}{LCs^2 + C(R_s + R_r)s + (1 - 2D)^2} \tag{28}$$

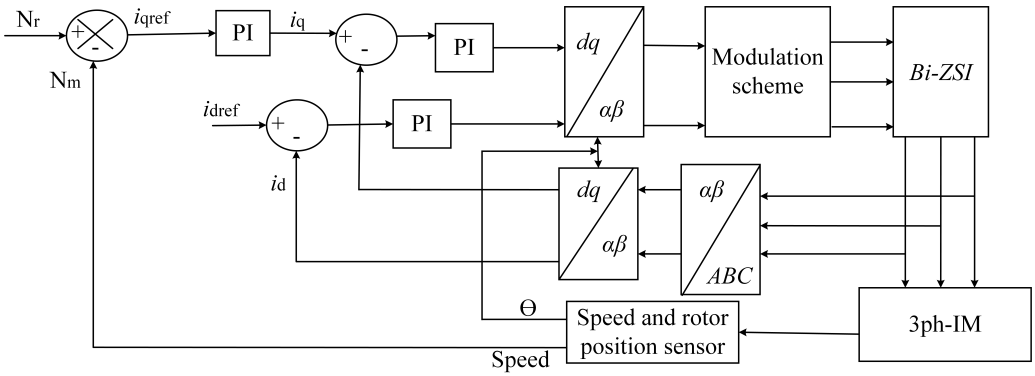

Figure 7. Control scheme of the Proposed fault-tolerant strategy.

The schematic structure of the above-mentioned fault-tolerant strategy and the control scheme is shown in Figure 8.

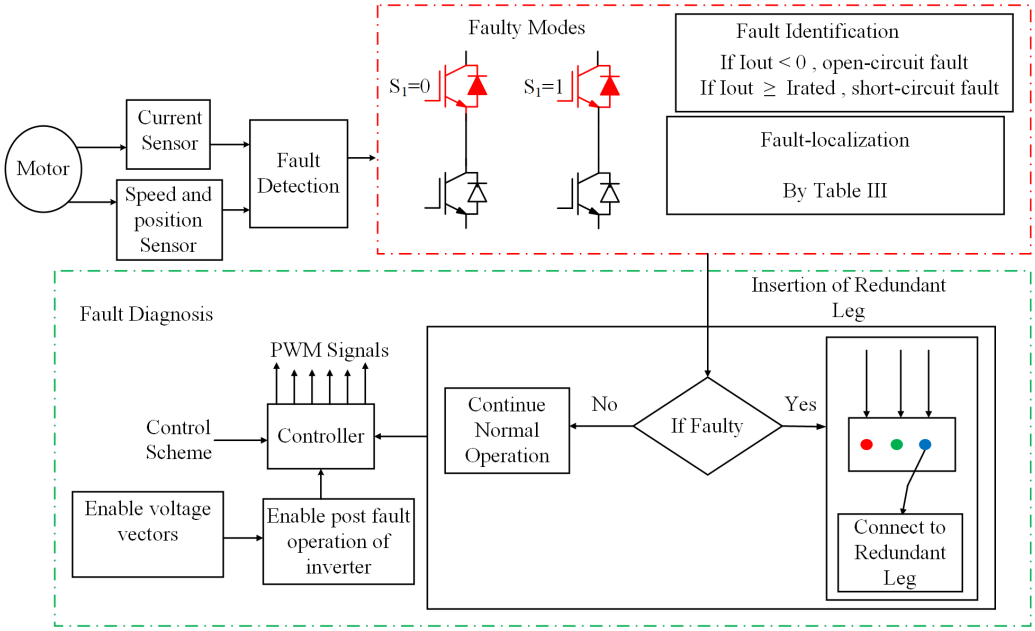

Figure 8. Schematic structure of the proposed fault-tolerant scheme.

4. Simulation Results

Several case studies are conducted using MATLAB/Simulink under different operating conditions to validate the efficacy of the proposed system. The system parameters are given in Table 2. Firstly, the normal operation of the proposed system is observed. Secondly, a comprehensive study of the variation in current and voltage under faulty conditions is analyzed. The case studies of this section are given as follows:

4.1. Normal Operation

The current and voltage waveforms under normal operation are given in Figure 9a. It is found that due to the proposed control methods, the system provides ripple-free output to the motor terminals.

4.2. Faulty Operation

4.2.1. Open-Circuit Fault

In this paper, the open-circuit fault is injected on IGBTs of phase-A. The simulation waveforms for the open-circuit failure of switches in phase-A are shown in Figure 9b. It is

observed that one-half of the positive cycle is clipped due to the open-circuit fault in the upper IGBT of phase-A. Alternatively, due to the two-switch failure in phase-A, the output current is zero.

4.2.2. Short-Circuit Fault

The simulation results of the output current of the proposed BiZSI-fed induction motor drive system for switch failure due to short-circuit in phase-A are shown in Figure 9c. It is observed that there is a sudden rise in the peak value of the output current due to the short-circuit fault in the upper IGBT of phase-A of the BiZSI system. These sudden current rises are not suitable for high-speed IGBT switching. Additionally, due to the two-switch failure in the same leg, the current across Phase-A is zero.

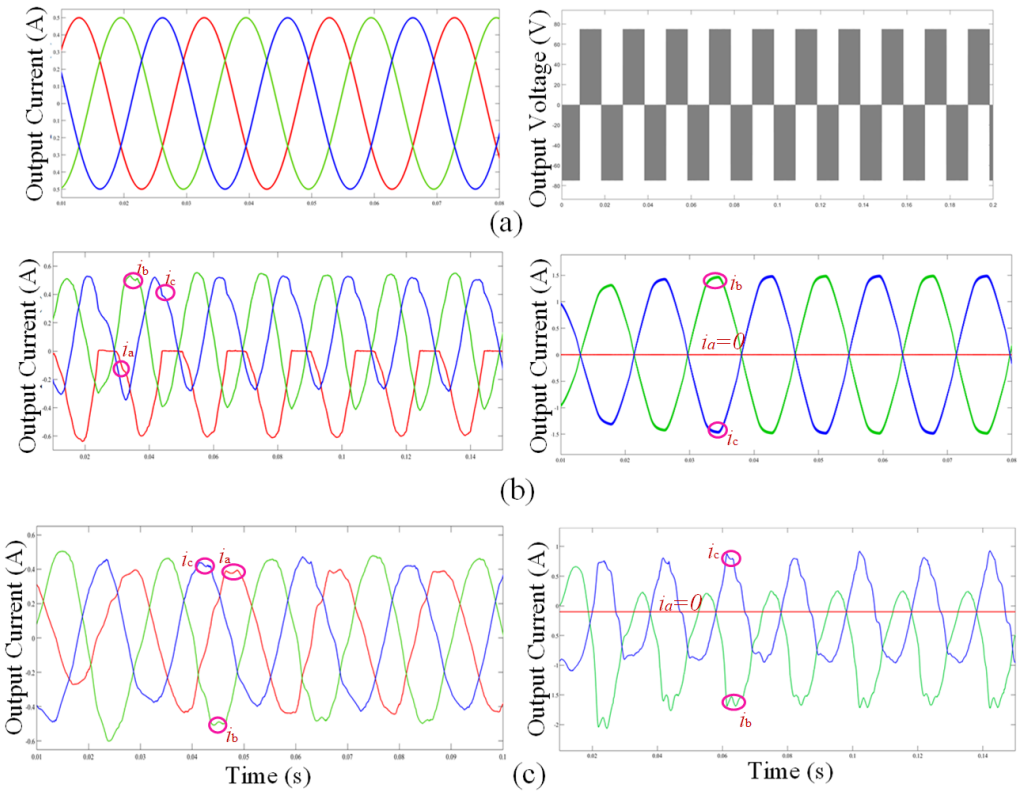

Figure 9. Simulation waveforms: (**a**) normal operation, (**b**) open-circuit fault, and (**c**) short-circuit fault.

The above analysis shows that the motor-drive system is not suitable for operation during faulty conditions.

4.3. Post-Fault Operation

The major disadvantage of switch failures is that they introduce high transients resulting in either zero or unbalanced three-phase currents. These variations in the currents are not recommended for the motor drive system. Hence, with the variable speed and load conditions of motor drives, the fault detection and protection from the high rise of currents should quickly come into action. Upon the detection of fault, the fault diagnosis strategy comes into action and the motor current is maintained to the rated value. The proposed current compensation approach, as described in Section 3, results in service continuity, even in the event of faults.

The high current transients during short-circuit faults are not suitable for the proposed low-voltage experimental setup in the laboratory and such faults are turned into open-circuit faults by the isolating circuit. They are handled by the proposed diagnosis method.

Hence, the fault-diagnosis characteristics are shown only during open-circuit switch failure. The output current response under fault-tolerant operation is shown in Figure 10.

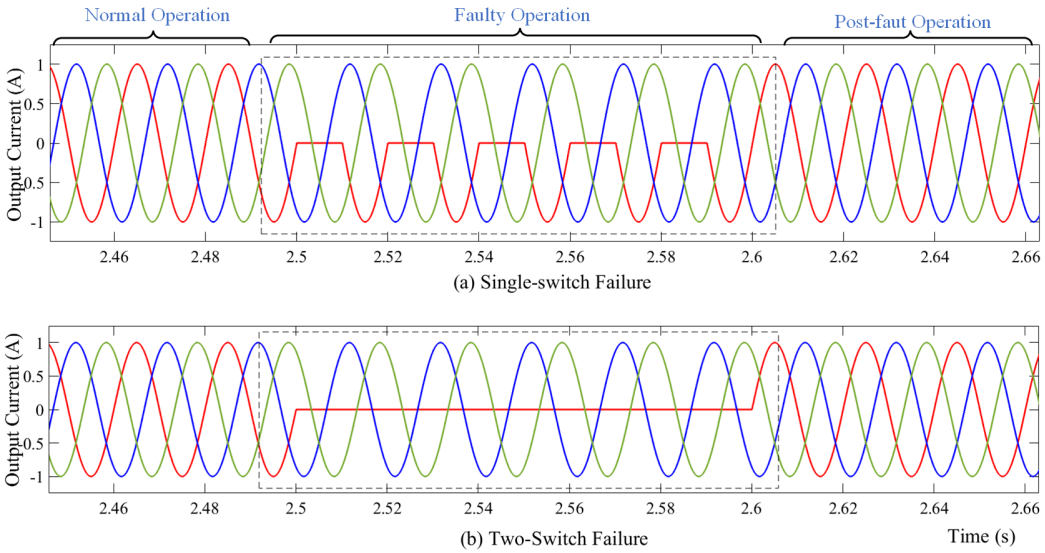

Figure 10. Simulation waveform of output currents during fault-tolerant operation: (**a**) Single-switch failure, (**b**) Two-switch failure.

5. Experimental Results

A low-voltage hardware prototype, as shown in Figure 11, is built in the laboratory to validate the simulation results of the proposed fault-tolerant scheme for the BiZSI-fed induction motor drive.

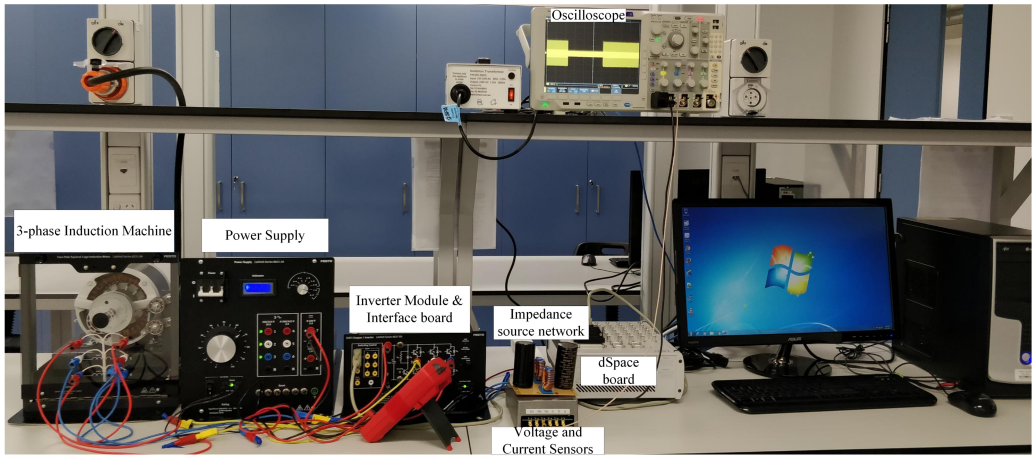

Figure 11. Experimental setup.

The high-gain modulation control scheme for the BiZSI is implemented in Simulink and interfaced to the Labvolt Inverter module with modifications to the internal circuit to support shoot-through and non-shoot-through states simultaneously. The inverter module switching section allows 0/5 V pulse signals compatible control unit to be applied to the gate circuits of the IGBTs. The IGBTs are able to withstand high temperatures with specifications of 600 V. The ac waveform obtained from the inverter module is fed to the 1.75 kW three-phase induction-machine. The parameters of the machine model are listed in Table A2 in the Appendix A. The bidirectional switch can withstand a peak voltage of 400 V during reverse flow of power. A dSPACE 1102 board is used to control the inverter. The interface board between the dSPACE and the inverter provides the control algorithm for fault-tolerant operation.

5.1. Normal Operation

The experimental results for the built prototype under normal operation are shown in Figure 12a.

5.2. Faulty Operation

Similar to the simulation analysis, the faults are injected in the phase-A IGBT of the inverter module.

5.2.1. Open-Circuit Fault

During an open-circuit fault, the output current waveforms are shown in Figure 12b. From Figure 12b, it is found that the characteristics of output current waveforms are similar to the simulation results. The negative half is clipped for single-switch failure in phase-A and zero current flows during two switch failure in phase-A.

5.2.2. Short-Circuit Fault

The experimental results for the switch failure under a short-circuit fault are shown in Figure 12c. It is evident from Figure12c that there is sudden rise of current during single- and two-switch failures due to the short-circuit fault. The motor drive system can be at high risk with the progression of such faults.

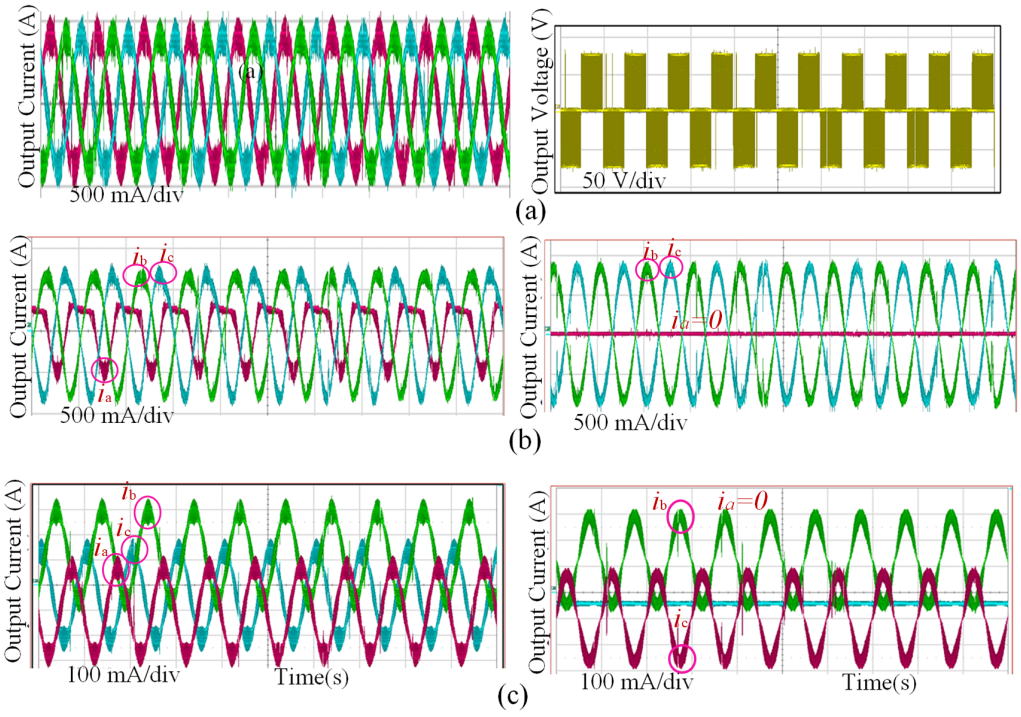

Figure 12. Experimental waveforms: (**a**) normal operation, (**b**) open-circuit fault, and (**c**) short-circuit fault.

5.3. Post-Fault Operation

The aim of this study is to investigate the efficacy of the proposed fault-tolerant strategy in maintaining the post-fault characteristics of the motor identical to the normal operation. Figure 13 demonstrates the output current response of the proposed motor drive under pre-fault, faulty, and post-fault operation. For the experimental analysis, open-circuit faults are injected at t = 2 s. Once a fault is detected in the system, the fault diagnostic strategy will be activated. With the proposed fault-tolerant topology the motor is brought back to the normal operation at t = 2.1 s. It is worth highlighting that a response time of 100ms, as shown in Figure13, is achieved during the fault-detection and diagnosis operation.

Though it requires nearly one fundamental cycle, it is acceptable in industrial applications involving automotives [53,54]. In all, the above experimental tests have validated the theoretical analysis.

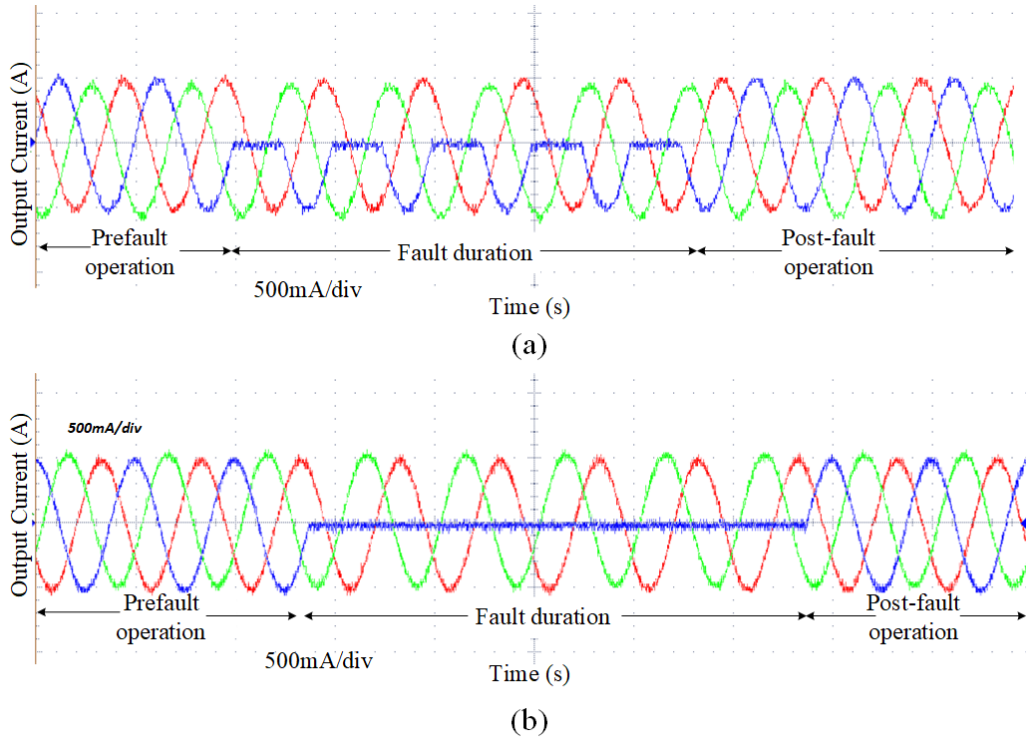

Figure 13. Experimental results under pre-fault, faulty, and post-fault operation (**a**) single-switch failure, and (**b**) two-switch failure.

6. Performance Evaluation for Vehicular Application

6.1. Motor Performance

To demonstrate the effectiveness of the proposed strategy for the motor drives, the induction motor torque-speed characteristics are plotted and shown in Figure 14. It can be observed that the motor characteristics under the post-fault operation are identical to the healthy operation. Hence, it is safe to implement the proposed fault-tolerant scheme for the considered BiZSI-fed induction motor drive system.

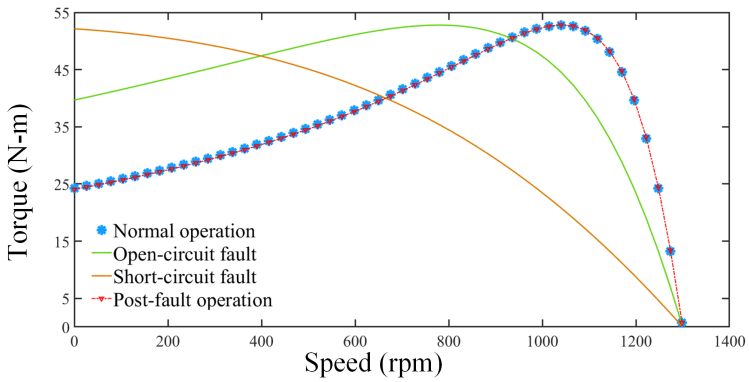

Figure 14. Torque-speed characteristics of the induction motor under fault-tolerant operation.

6.2. Speed Response

The dip in speed of the motor is monitored for the experimental study. The motor drive operates under the rated speed in the event of faults, and restores back to the rated

value after implementing the proposed fault-tolerant strategy. The speed characteristics of the induction motor drive are shown in Figure 15. The speed response of the induction motor is observed for two instances of the faults for the experimental prototype. In each event of a fault, the motor is brought back to the rated operation in due time.

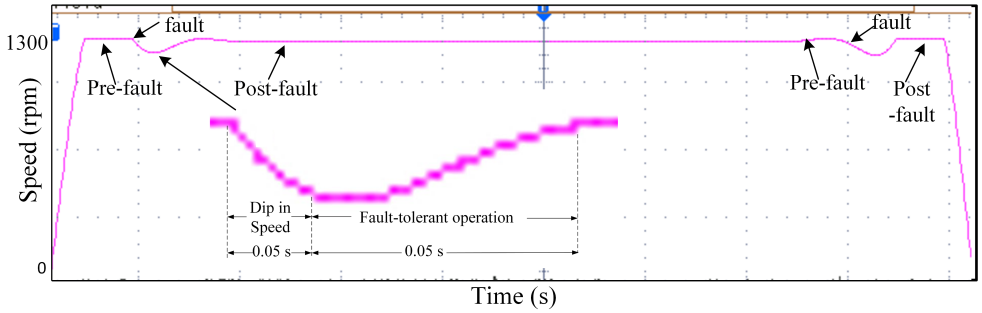

Figure 15. Speed response under fault-tolerant operation.

6.3. Harmonic Response

To verify the efficacy of the proposed scheme in terms of harmonics, an analysis of the total harmonic distortion (THD) magnitudes for the above-mentioned cases is shown in Table 5. The experimental results indicate that the values of THD are higher, but are under the acceptable values of IEEE standard 519-2014. The impact of the negative sequence is reduced and the motor rotates with sufficient field supply. This advantage proves the suitability of the proposed method for vehicular application.

Table 5. Harmonic Spectrum Results of Load Currents in phase-A.

	THD (%)	
Case	**Simulation**	**Experimental**
Normal Operation	0.79	1.56
Open-circuit fault	78.06	82.63
Short-circuit fault	45.02	49.60
Proposed fault-tolerant strategy	1.41	2.36

6.4. Torque Response

The motor performance is evaluated experimentally by measuring the torque response. The variation in torque is presented in Figure 16. It can be observed from Figure 16 that the torque decreases in the event of fault. Upon the detection of a fault, the diagnosis strategy is implemented and the torque magnitude is compensated to the rated value. Therefore, the motor continues to operate in the event of faults.

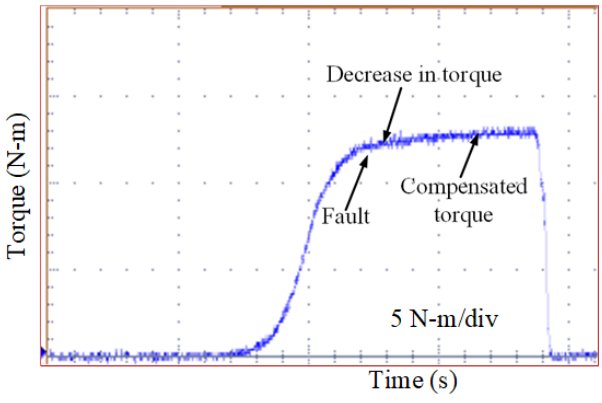

Figure 16. Torque response under fault-tolerant operation.

6.5. Efficiency Curve

The measurement for the power throughput is performed and the efficiency curve for normal and fault-tolerant operation is plotted in Figure 17.

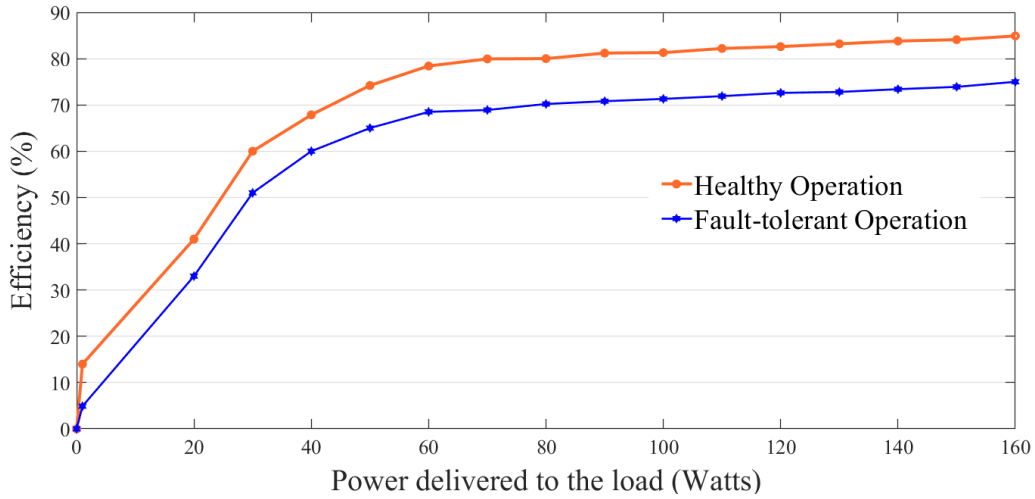

Figure 17. Efficiency curve.

The effectiveness of the service continuity has been studied through the above-listed experimental analysis. The motor drive system continues to be in operation, even under the events of faults. It should be noted that the available output after the fault-tolerant operation is nearly equal to 80% of the normal operation. The achieved results have demonstrated the feasibility of the proposed strategy for improving the reliability of the motor drive system.

6.6. Motor Characterises for Vehicular Application

The speed-torque characteristics of the IM is plotted in Figure 18 for a New European Driving Cycle (NEDC) in order to prove the suitability of the proposed drive for vehicular application particularly electric vehicles. The driving cycle is a set of data points which represents speed-time profile resembling the real-world driving pattern. This driving cycle plot considers the motor parameter variations in acceleration, deceleration, and braking. The driving cycle parameters are listed in Table A1 in Appendix A.

It can be seen in Figure 18 that the estimated speed tracks the reference speed with a a negligible error. Similarly, the torque profile shown in Figure 18 shows that the measured torque follows its reference generated by the speed PI controller with insignificant torque ripples during operation. The driving cycle response proves that the IM drive delivers improved performance in steady state operation over the variables' speed range. The achieved results have less ripples for rapid speed-torque variations with negligible steady-state error.

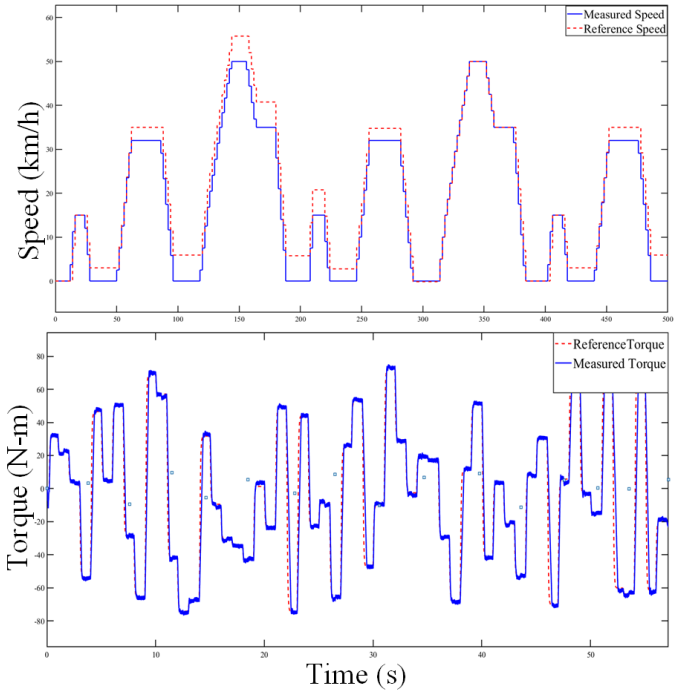

Figure 18. Driving cycle response for vehicular application.

7. Comparative Analysis

To validate the potential of the proposed fault-tolerant scheme, a comparative analysis of the performance of the designed scheme with that of other similar strategies utilized in the industries is presented in Table 6. It is implied in Table 6 that the proposed fault-tolerant strategy is efficient and has lower complexity in the circuit design in comparison to other strategies.

Table 6. Comparative analysis of proposed fault-tolerant strategy with other strategies.

Strategy	OC Switch Fault Covered	SC Switch Fault Covered	Complexity	Properties
[55]	Yes	Yes	Average	Able to force common-mode voltage to zero Ride-through capability during switch failure
[56]	Yes	Yes	Complex	Enabling of the Z-source CHB is required Hardware complexity
[57]	No	No	Complex	Cascaded connection required Access to neutral point is required
[58]	Yes	Yes	Complex	Only for multilevel converter topology Focused on phase-shift compensation
[59]	Yes	Yes	Average	Requires extra hardware Access to dc-bus mid-point is not required
Proposed Strategy	Yes	Yes	Simple	Applicable to motor drive No capacitor balancing issues Fast and efficient post-fault strategy Lower conduction losses

In addition, a comparison of the recovery time for similar fault-tolerant strategies is plotted in Figure 19 to validate the effectual speedy-recovery characteristics of the proposed fault-tolerant system.

This comparative study is obtained through simulation studies performed under identical test conditions performed on two popular converter-inverter topologies and the proposed system utilized for three-phase inverter-fed induction motor drives:

(i) Traditional Z-source inverter;
(ii) Cascaded H-bridge inverter.

These topologies are simulated with parameters: three-phase line voltage, V = 230 V, line impedance = 4%, load = three-phase 230 V, 1 kW induction motor.

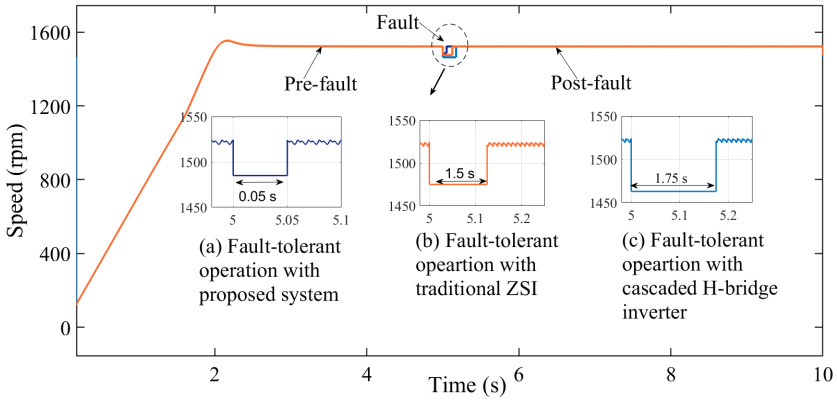

Figure 19. Recovery time characteristics of fault-tolerant strategies.

It is clearly inferred from Figure 19 that the proposed fault-tolerant strategy facilitates a speedy recovery compared to traditional fault-tolerant strategies implemented in industrial applications. As per simulation studies, the time taken to detect and diagnose the fault is 0.05 s for the proposed system. On the other hand, the time required to diagnose the fault in the traditional Z-source inverter system is 1.5 s, while it is 1.75 s for the cascaded H-bridge inverter system.

Based on the above study, the proposed system has the following advantages for vehicular applications.

1. The proposed fault-tolerant strategy emphasizes that the post-fault speed characteristics are not sluggish. In addition, the control scheme offers voltage balancing of the DC-link capacitors under sudden load variations. This feature specifically suits high-voltage vehicle drives.
2. The proposed converter topology facilitates a bidirectional flow of power. This added advantage can recover the kinetic energy of the vehicle during regenerative braking.
3. The obtained results are characterized by a less distorted output. This feature eliminates the problem of harmonic resonances due to the passive LC parameters of the system. The low harmonic distortion improves the utilization rate of the motor drive.
4. The economical design and implementation of the proposed fault modulation scheme can supersede the conventional voltage-based method since low-voltage switching devices with lower conduction losses are used. This results in the low weight and volume of the proposed experimental prototype.

8. Conclusions

In this paper, an efficient fault-tolerant strategy characterized by speedy recovery for a BiZSI-fed induction-motor drive, is presented. The proposed modulation scheme provides high-gain voltage output. The fault-detection schemes for open-circuit and short-circuit faults are logical and cost-effective. The control scheme facilitates the continuous operation after a fault occurrence and is suitable for the reliable operation of the induction motor drive. The detection time and diagnosis duration are minimal to avoid any delays in operation during switch failures. The control scheme is promising in comparison to other similar strategies and can be applied to other AC motors. The experimental results validate the merits of the strategy for the system. The post-fault operation evaluation depicts similar characteristics as a healthy operation, which makes the motor drive suitable for vehicular applications. The proposed method is highly safe for crucial applications of motors.

Author Contributions: V.S. conceived, designed and performed the simulation and experimental evaluations and was responsible for preparing the original draft of this paper; M.J.H. and S.M. supervised for the development of the power topology and conceptual solution and were responsible for the reviewing and editing of this paper. All authors have read and agreed to the published version of the manuscript.

Funding: This research received no external funding.

Institutional Review Board Statement: Not Applicable.

Informed Consent Statement: Not Applicable.

Data Availability Statement: Not Applicable.

Conflicts of Interest: The authors declare no conflict of interest.

Abbreviations

The following abbreviations are used in this manuscript:

IGBT	Insulated Gate Bipolar Transistor
THD	Total Harmonic Distortion
CVR	Capacitor Voltage Ripple
SDP	Switching Device Power
TRIAC	Triode for Alternating Current

Appendix A

Table A1. Driving Cycle Parameters.

Symbol	Parameter	Value
S	Distance Covered	10 km
v	Average Speed	30 km/h
v_m	Maximum speed	75 km/h
a	Maximum Acceleration	2.3 m/s^2
a	Maximum Deceleration	−2.1 m/s^2
T	Idle Time	170 s

Table A2. Specifications of the Machine.

Symbol	Device	Ratings
V_s	Stator voltage	220 V, 50 Hz
P_m	Mechanical power	1.75 kW
N	Nominal speed	1380 rpm
I_{rated}	Nominal current	0.52 A
J	Moment of inertia	0.06 kg.m^2
R_s	Stator resistance	1.1 Ω
R_r	Rotor resistance	1.1 Ω
L_s	Stator inductance	170 mH
L_r	Rotor inductance	170 mH
T_{rated}	Nominal torque	13.3 N.m
p	Pole pairs	4

References

1. Emadi, A.; Lee, Y.J.; Rajashekara, K. Power Electronics and Motor Drives in Electric, Hybrid Electric, and Plug-In Hybrid Electric Vehicles. *IEEE Trans. Ind. Electron.* **2008**, *55*, 2237–2245. [CrossRef]
2. Pellegrino, G.; Vagati, A.; Boazzo, B.; Guglielmi, P. Comparison of Induction and PM Synchronous Motor Drives for EV Application Including Design Examples. *IEEE Trans. Ind. Appl.* **2012**, *48*, 2322–2332. [CrossRef]
3. Yang, Z.; Shang, F.; Brown, I.P.; Krishnamurthy, M. Comparative Study of Interior Permanent Magnet, Induction, and Switched Reluctance Motor Drives for EV and HEV Applications. *IEEE Trans. Transp. Electrif.* **2015**, *1*, 245–254. [CrossRef]

4. Devanshu, A.; Singh, M.; Kumar, N. An Improved Nonlinear Flux Observer Based Sensorless FOC IM Drive With Adaptive Predictive Current Control. *IEEE Trans. Power Electron.* **2020**, *35*, 652–666. [CrossRef]
5. Emadi, A.; Rajashekara, K.; Williamson, S.S.; Lukic, S.M. Topological overview of hybrid electric and fuel cell vehicular power system architectures and configurations. *IEEE Trans. Veh. Technol.* **2005**, *54*, 763–770. [CrossRef]
6. Nemeth, T.; Bubert, A.; Becker, J.N.; De Doncker, R.W.; Sauer, D.U. A Simulation Platform for Optimization of Electric Vehicles With Modular Drivetrain Topologies. *IEEE Trans. Transp. Electrif.* **2018**, *4*, 888–900. [CrossRef]
7. Banerjee, D.; Ranganathan, V.T. Load-Commutated SCR Current-Source-Inverter-Fed Induction Motor Drive With Sinusoidal Motor Voltage and Current. *IEEE Trans. Power Electron.* **2009**, *24*, 1048–1061. [CrossRef]
8. Kastha, D.; Majumdar, A.K. An improved starting strategy for voltage-source inverter fed three phase induction motor drives under inverter fault conditions. *IEEE Trans. Power Electron.* **2000**, *15*, 726–732. [CrossRef]
9. Sebastian C, R.; Rajeevan, P.P. Load-Commutated SCR-Based Current Source Inverter Fed Induction Motor Drive With Open-End Stator Windings. *IEEE Trans. Ind. Electron.* **2018**, *65*, 2031–2038. [CrossRef]
10. Kadrine, A.; Tir, Z.; Malik, O.P.; Hamida, M.A.; Reatti, A.; Houari, A. Adaptive non-linear high gain observer based sensorless speed estimation of an induction motor. *J. Frankl. Inst.* **2020**, *357*, 8995–9024. doi: 10.1016/j.jfranklin.2020.06.013. [CrossRef]
11. Sher, H.A.; Addoweesh, K.E.; Khan, Y.; Kashif, S.A.R. Performance of inverter fed induction motor under open circuit DC link capacitor. In Proceedings of the IECON 2012—38th Annual Conference on IEEE Industrial Electronics Society, Montreal, QC, Canada, 25–28 October 2012; pp. 651–655. [CrossRef]
12. Peng, F. Z-source inverter. *IEEE Trans. Ind. Appl.* **2003**, *39*, 504–510. [CrossRef]
13. Fang Zheng Peng.; Joseph, A.; Jin Wang.; Miaosen Shen.; Lihua Chen.; Zhiguo Pan.; Ortiz-Rivera, E.; Yi Huang. Z-source inverter for motor drives. *IEEE Trans. Power Electron.* **2005**, *20*, 857–863. [CrossRef]
14. Tidke, R.; Chowdhury, A. Quasi ZSI-Fed Sliding Mode Control-based Indirect Field-Oriented Control of IM Using PI-Fuzzy Logic Speed Controller. *Electrica* **2021**, *22*, 70–83. doi: 10.5152/electrica.2021.21081. [CrossRef]
15. Sonandkar, S.; Selvaraj, R.; Chelliah, T.R. Fault Tolerant Capability of Battery Assisted Quasi-Z-Source Inverter Fed Five Phase PMSM Drive for Marine Propulsion Applications. In Proceedings of the 2020 IEEE International Conference on Power Electronics, Drives and Energy Systems (PEDES), Jaipur, India, 16–19 December 2020; pp. 1–6. [CrossRef]
16. Sharma, V.; Saini, P.; Garg, S.; Negi, B. Comparative analysis of VSI, CSI and ZSI fed induction motor drive system. In Proceedings of the 2016 3rd International Conference on Computing for Sustainable Global Development (INDIACom), New Delhi, India, 16–18 March 2016; pp. 1188–1191.
17. de Araujo Ribeiro, R.L.; Jacobina, C.B.; da Silva, E.R.C.; Lima, A.M.N. Fault-tolerant voltage-fed PWM inverter AC motor drive systems. *IEEE Trans. on Ind. Electron.* **2004**, *51*, 439–446. [CrossRef]
18. Yu, Y.; Zhao, Y.; Wang, B.; Huang, X.; Xu, D. Current Sensor Fault Diagnosis and Tolerant Control for VSI-Based Induction Motor Drives. *IEEE Trans. Power Electron.* **2018**, *33*, 4238–4248. [CrossRef]
19. Melo, V.F.M.B.; Jacobina, C.B.; Rocha, N.; Braga-Filho, E.R. Fault Tolerance Performance of Two Hybrid Six-Phase Drive Systems Under Single-Phase Open-Circuit Fault Operation. *IEEE Trans. Ind. Appl.* **2019**, *55*, 2973–2983. [CrossRef]
20. Tousizadeh, M.; Che, H.S.; Selvaraj, J.; Rahim, N.A.; Ooi, B. Performance Comparison of Fault-Tolerant Three-Phase Induction Motor Drives Considering Current and Voltage Limits. *IEEE Trans. Ind. Electron.* **2019**, *66*, 2639–2648. [CrossRef]
21. Errabelli, R.R.; Mutschler, P. Fault-Tolerant Voltage Source Inverter for Permanent Magnet Drives. *IEEE Trans. Power Electron.* **2012**, *27*, 500–508. [CrossRef]
22. Yao, F.; Wang, B.; Li, Z.; Peng, Y. Reliability study on DC-link capacitor in fault states of VSI in elective vehicle. *J. Eng.* **2019**, *2019*, 2544–2550. doi: 10.1049/joe.2018.8612. [CrossRef]
23. Zhang, H.; Zhao, W.; Wang, J. Fault-Tolerant Control for Electric Vehicles With Independently Driven in-Wheel Motors Considering Individual Driver Steering Characteristics. *IEEE Trans. Veh. Technol.* **2019**, *68*, 4527–4536. [CrossRef]
24. Sher, H.A.; Addoweesh, K.E.; Khalid, Z.; Khan, Y. Theoretical and experimental analysis of inverter fed induction motor system under DC link capacitor failure. *J. King Saud Univ. -Eng. Sci.* **2017**, *29*, 103–111. doi: 10.1016/j.jksues.2015.06.001. [CrossRef]
25. Li, J.N.; Wang, A.M.; Miao, K.Z.; Li, L.S. Failure-distribution-dependent H∞ fuzzy fault-tolerant control for multiple-degree-of-freedom nonlinear bilateral teleoperation system. *J. Frankl. Inst.* **2020**, *357*, 13511–13533. doi: 10.1016/j.jfranklin.2020.10.005. [CrossRef]
26. Zhang, W.; Xu, D.; Enjeti, P.N.; Li, H.; Hawke, J.T.; Krishnamoorthy, H.S. Survey on Fault-Tolerant Techniques for Power Electronic Converters. *IEEE Trans. Power Electron.* **2014**, *29*, 6319–6331. [CrossRef]
27. Yepes, A.G. A Comprehensive Survey on Fault Tolerance in Multiphase AC Drives, Part 1: General Overview Considering Multiple Fault Types. *Machines* **2022**, *10*, 208. doi: 10.3390/machines10030208. [CrossRef]
28. Li, S.; Xu, L. Strategies of fault tolerant operation for three-level PWM inverters. *IEEE Trans. Power Electron.* **2006**, *21*, 933–940. [CrossRef]
29. Mirafzal, B. Survey of Fault-Tolerance Techniques for Three-Phase Voltage Source Inverters. *IEEE Trans. Ind. Electron.* **2014**, *61*, 5192–5202. [CrossRef]
30. Wang, N.; Pan, X.; Su, S.F. Finite-time fault-tolerant trajectory tracking control of an autonomous surface vehicle. *J. Frankl. Inst.* **2020**, *357*, 11114–11135. doi: 10.1016/j.jfranklin.2019.05.016. [CrossRef]
31. Abdelhakim, A.; Davari, P.; Blaabjerg, F.; Mattavelli, P. An improved modulation strategy for the three-phase Z-source inverters (ZSIs). In Proceedings of the 2017 IEEE Energy Conversion Congress and Exposition (ECCE), Cincinnati, OH, USA, 1–5 October 2017; pp. 4237–4243. [CrossRef]

32. Abdelhakim, A.; Blaabjerg, F.; Mattavelli, P. Modulation Schemes of the Three-Phase Impedance Source Inverters—Part I: Classification and Review. *IEEE Trans. Ind. Electron.* **2018**, *65*, 6309–6320. [CrossRef]
33. Abdelhakim, A.; Blaabjerg, F.; P.Mattavelli. Modulation Schemes of the Three-Phase Impedance Source Inverters—Part II: Comparative Assessment. *IEEE Trans. Ind. Electron.* **2018**, *65*, 6321–6332. [CrossRef]
34. Lee, H.J.; Jung, S.; Sul, S.K. A current controller design for current source inverter-fed PMSM drive system. In Proceedings of the 8th International Conference on Power Electronics—ECCE Asia, Jeju, Korea, 30 May–3 June 2011; pp. 1364–1370. [CrossRef]
35. Yang, S.; Tong, C.; Sui, Y.; Yin, Z.; Zheng, P. Current-Source Inverter Fed Five-Phase PMSM Drives With Pentagon Stator Winding Considering SVM Scheme, Resonance Damping, and Fault Tolerance. *IEEE Trans. Ind. Electron.* **2022**, 1–11. [CrossRef]
36. Rajakaruna, S.; Jayawickrama, Y.R.L. Designing impedance network of Z-source inverters. In Proceedings of the 2005 International Power Engineering Conference, Singapore, 8 May 2005; Volume 2, pp. 962–967. [CrossRef]
37. Liu, Y.; Ge, B.; Abu-Rub, H.; Peng, F.Z. Overview of Space Vector Modulations for Three-Phase Z-Source/Quasi-Z-Source Inverters. *IEEE Trans. Power Electron.* **2014**, *29*, 2098–2108. [CrossRef]
38. Diab, M.S.; Elserougi, A.A.; Massoud, A.M.; Abdel-Khalik, A.S.; Ahmed, S. A Pulsewidth Modulation Technique for High-Voltage Gain Operation of Three-Phase Z-Source Inverters. *IEEE J. Emerg. Sel. Top. Power Electron.* **2016**, *4*, 521–533. [CrossRef]
39. Bakar, M.S.; Rahim, N.A.; Ghazali, K.H.; Hanafi, A.H.M. Z-source inverter pulse width modulation: A survey. In Proceedings of the International Conference on Electrical, Control and Computer Engineering 2011 (InECCE), Kuantan, Malaysia 21–22 June 2011; pp. 313–316.
40. Sharma, V.; Hossain, M.J.; Ali, S.M.N. Fault Protection Technique for ZSI-fed Single-Phase Induction Motor Drive System. In Proceedings of the 2018 IEEE Region Ten Symposium (Tensymp), Sydney, NSW, Australia, 4–6 July 2018; pp. 30–35. [CrossRef]
41. Ellabban, O.; Van Mierlo, J.; Lataire, P. A comparative study of different control techniques for an induction motor fed by a Z-source inverter for electric vehicles. In Proceedings of the 2011 International Conference on Power Engineering, Energy and Electrical Drives, Malaga, Spain, 11–13 May 2011; pp. 1–7.
42. Ellabban, O.; Van Mierlo, J.; Lataire, P. Comparison between different PWM control methods for different Z-source inverter topologies. In Proceedings of the 2009 13th European Conference on Power Electronics and Applications, Barcelona, Spain, 8–10 September 2009; pp. 1–11.
43. Thurlbeck, A.P.; Cao, Y. A Mission Profile-Based Reliability Modeling Framework for Fault-Tolerant Electric Propulsion. *IEEE Trans. Ind. Appl.* **2022**, *58*, 2312–2323. [CrossRef]
44. Sharma, V.; Hossain, M.J.; Ali, S.M.N.; Kashif, M. Bi-directional TRIAC fault-protection technique for Z-source half-bridge converter-fed AC motor Drives. In Proceedings of the 2018 Australasian Universities Power Engineering Conference (AUPEC), Auckland, New Zealand, 27–30 November 2018; pp. 1–6. [CrossRef]
45. Hubbi, W.; Goldberg, O. A new method for quality monitoring of induction motors. *IEEE Trans. Energy Convers.* **1993**, *8*, 726–731. [CrossRef]
46. Medarametla, J.; Cox, M.; Baghzouz, Y. Calculations and measurements of the Unity Plus three-phase induction motor. *IEEE Trans. Energy Convers.* **1992**, *7*, 732–738. [CrossRef]
47. Kastha, D.; Bose, B. Fault mode single-phase operation of a variable frequency induction motor drive and improvement of pulsating torque characteristics. *IEEE Trans. Ind. Electron.* **1994**, *41*, 426–433. [CrossRef]
48. Li, B.; Shi, S.; Wang, B.; Wang, G.; Wang, W.; Xu, D. Fault Diagnosis and Tolerant Control of Single IGBT Open-Circuit Failure in Modular Multilevel Converters. *IEEE Trans. Power Electron.* **2016**, *31*, 3165–3176. [CrossRef]
49. Farhadi, M.; Fard, M.T.; Abapour, M.; Hagh, M.T. DC–AC Converter-Fed Induction Motor Drive With Fault-Tolerant Capability Under Open- and Short-Circuit Switch Failures. *IEEE Trans. Power Electron.* **2018**, *33*, 1609–1621. [CrossRef]
50. Sleszynski, W.; Nieznanski, J.; Cichowski, A. Open-Transistor Fault Diagnostics in Voltage-Source Inverters by Analyzing the Load Currents. *IEEE Trans. Ind. Electron.* **2009**, *56*, 4681–4688. [CrossRef]
51. Lu, B.; Sharma, S.K. A Literature Review of IGBT Fault Diagnostic and Protection Methods for Power Inverters. *IEEE Trans. Ind. Appl.* **2009**, *45*, 1770–1777.
52. Rothenhagen, K.; Fuchs, F.W. Performance of diagnosis methods for IGBT open circuit faults in three phase voltage source inverters for AC variable speed drives. In Proceedings of the 2005 European Conference on Power Electronics and Applications, Dresden, Germany, 11–14 September 2005.
53. Guzman, H.; Barrero, F.; Duran, M.J. IGBT-Gating Failure Effect on a Fault-Tolerant Predictive Current-Controlled Five-Phase Induction Motor Drive. *IEEE Trans. Ind. Electron.* **2015**, *62*, 15–20. [CrossRef]
54. Diallo, D.; Benbouzid, M.E.H.; Makouf, A. A fault-tolerant control architecture for induction motor drives in automotive applications. *IEEE Trans. Veh. Techn.* **2004**, *53*, 1847–1855. [CrossRef]
55. Le Duc, D.; Hong, S.; Lee, D.C. Fault detection and tolerant control for flying-capacitor modular multilevel converters feeding induction motor drives. *J. Power Electron.* **2022**, *22*, 947–958. doi: 10.1007/s43236-022-00425-x. [CrossRef]
56. Aleenejad, M.; Ahmadi, R. Fault-tolerant multilevel cascaded H-bridge inverter using impedance-sourced network. *IET Power Electron.* **2016**, *9*, 2186–2195. doi: 10.1049/iet-pel.2016.0033. [CrossRef]
57. Haji-Esmaeili, M.M.; Naseri, M.; Khoun-Jahan, H.; Abapour, M. Fault-Tolerant and Reliable Structure for a Cascaded Quasi-Z-Source DC–DC Converter. *IEEE Trans. Power Electron.* **2017**, *32*, 6455–6467. [CrossRef]

58. Aleenejad, M.; Mahmoudi, H.; Ahmadi, R. A Fault-Tolerant Strategy Based on Fundamental Phase-Shift Compensation for Three-Phase Multilevel Converters With Quasi-Z-Source Networks With Discontinuous Input Current. *IEEE Trans. Power Electron.* **2016**, *31*, 7480–7488. [CrossRef]
59. Fernão Pires, V.; Cordeiro, A.; Foito, D.; Martins, J.F. Quasi-Z-Source Inverter With a T-Type Converter in Normal and Failure Mode. *IEEE Trans. Power Electron.* **2016**, *31*, 7462–7470. [CrossRef]